

Tailoring the Morphology of MTW Zeolite Mesocrystals: Intertwined Classical/Non-classical Crystallization

Yang Zhao, Hongbin Zhang, Peicheng Wang, Fangqi Xue, Zhaoqi Ye, Yahong Zhang, and Yi Tang

Chem. Mater., **Just Accepted Manuscript** • DOI: 10.1021/acs.chemmater.6b03813 • Publication Date (Web): 28 Mar 2017

Downloaded from <http://pubs.acs.org> on March 30, 2017

Just Accepted

“Just Accepted” manuscripts have been peer-reviewed and accepted for publication. They are posted online prior to technical editing, formatting for publication and author proofing. The American Chemical Society provides “Just Accepted” as a free service to the research community to expedite the dissemination of scientific material as soon as possible after acceptance. “Just Accepted” manuscripts appear in full in PDF format accompanied by an HTML abstract. “Just Accepted” manuscripts have been fully peer reviewed, but should not be considered the official version of record. They are accessible to all readers and citable by the Digital Object Identifier (DOI®). “Just Accepted” is an optional service offered to authors. Therefore, the “Just Accepted” Web site may not include all articles that will be published in the journal. After a manuscript is technically edited and formatted, it will be removed from the “Just Accepted” Web site and published as an ASAP article. Note that technical editing may introduce minor changes to the manuscript text and/or graphics which could affect content, and all legal disclaimers and ethical guidelines that apply to the journal pertain. ACS cannot be held responsible for errors or consequences arising from the use of information contained in these “Just Accepted” manuscripts.

Tailoring the Morphology of MTW Zeolite Mesocrystals: Intertwined Classical/Non-classical Crystallization

Yang Zhao,^a Hongbin Zhang,^{a,*} Peicheng Wang,^a Fangqi Xue,^a Zhaoqi Ye,^a Yahong Zhang,^a Yi Tang^{a,*}

^aDepartment of Chemistry, Laboratory of Advanced Materials, Collaborative Innovation Center of Chemistry for Energy Materials and Shanghai Key Laboratory of Molecular Catalysis and Innovative Materials, Fudan University, Shanghai, 200433, China.

ABSTRACT: Morphology and porosity of zeolite play a significant role on the activity and selectivity of catalytic reactions. It is a dream to optionally modulate zeolite morphology by regulating the crystallization process on the basis of comprehensively understanding mechanisms. Herein, a series of MTW zeolite mesocrystals can be consciously fabricated with the morphologies from dense structure to loose one of oriented nanocrystallite-aggregate by changing H₂O/SiO₂ ratio. Their intertwined classical/non-classical crystallization processes are investigated comprehensively. The results indicate that the crystallization of MTW zeolite takes place by a chain of events including the formation of worm-like particles (WLPs), their aggregation and crystallization of aggregates. MTW with loose structure mainly crystallizes by an internal reorganization after a fast aggregation of WLPs in a concentrated system. On the other hand, the dense structure of MTW is obtained due to the co-occurrence of a coalescence of the participating WLPs during its crystal growth with slower rate in a dilute system. Moreover, the advantages of MTW with loose structure are confirmed through cumene cracking and 1,2,4-trimethylbenzenes transformation. This method could pave a way for the synthesis of other zeolites with diverse morphologies/mesoporosities via subtle regulation of crystallization pathway.

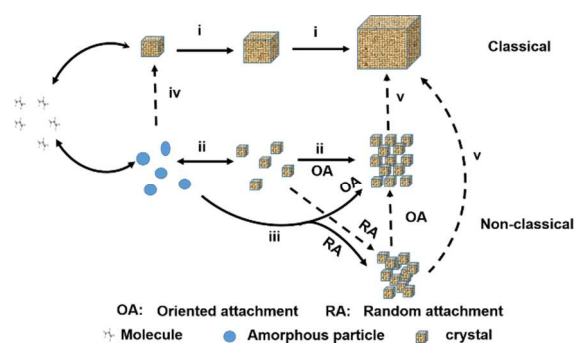
1. INTRODUCTION

Zeolites are a class of aluminosilicate crystals with specific microporous frameworks, which are significant candidates for catalysis, separation and adsorption,^{1,3} particularly, in petrochemical industry due to their distinctive acidity, shape selectivity and high hydrothermal stability.⁴ Due to diffusion limitation in the sole micropores of zeolites, the performances of catalytic reactions or adsorption often strongly depend on their crystal size, morphology and porosity.^{5,6} Especially for the zeolites with one-dimensional (1D) pore system, they usually suffer from a long diffusion path for the high crystal aspect ratios (length/width),⁷ such as MTW, TON, MOR, etc. In recent years, many efforts have been made to rationally design the crystal morphology/porosity of a given zeolite.⁸ Post-treatments are the conventional methods to tailor porosities of diverse zeolites.⁹⁻¹² Alternatively, designing exceptional templates is pervasively popular for directing the formation of zeolites with distinctive structures.¹³⁻¹⁶ In addition, adding some exotic additives, such as crystal-growth modifiers¹⁷⁻¹⁹ or seed crystals,^{6,20} can also fine-tune the crystal size and morphology through inhabiting some specific lattice planes or inducing the distinct dissolution-recrystallization process. Despite these elegant achievements, scientists are devoting themselves to develop a prospective approach for zeolite morphology modulation via directly controlling the crystallization kinetics by solely changing the synthesis conditions, such as sol composition, aging time, crystallization temperature and so on, as it is not only facilely executable but also economically feasible.^{21,22}

The crystallization mechanism of zeolite so far is still controversial because it is affected by multifactor during the multiple pathways.²³ However, the systematic understanding of crystallization mechanism is extraordinarily vital for subtle and controllable synthesis of zeolite. Based on the species of crystal-grown nutrients, crystallization mechanisms can be divided into two categories: classical and non-classical (Scheme 1).²⁴⁻²⁸ In a classical process, single crystal zeolites with smooth surface are formed generally via layer-by-layer addition of simple species to a pre-formed nucleus (path i).^{29,30} On the other hand, in a non-classical one, a special crystallization occurs by nanoparticle-by-nanoparticle attachment, where the nanoparticles could be crystalline (path ii)³¹ or amorphous (path iii).³² Interestingly, the aggregative nucleation and growth usually produce a mesoscopically structured crystal (i.e., "mesocrystal").³³ Such non-classical process has been reported for the formation of diverse three-dimensional (3D) ordered mesocrystals such as metal oxides,³⁴ magnetite³⁵ and proteins.³⁶ Recently, it has also been proposed as one of dominant mechanisms for elaborating the formation of polycrystalline or single-crystal-like zeolites by random- (RA)²⁰ or oriented-attachment (OA)³⁷⁻³⁹ of nanoparticles, respectively. However, these two pathways of classical and non-classical mechanisms may overlap or co-exist to some extent and the relative magnitudes may vary. For example, during crystallization, the amorphous nanoparticles can dissolve into simple species or even molecules and then add onto the pre-formed crystal nucleus (path iv);⁴⁰ And the disordered and ordered polycrystallites formed via paths ii and iii perhaps act as the intermediates for the formation of zeolite crystals with diverse morphologies/mesoporosities,

even forming an intact single crystal via rearrangement of nanocrystals or addition of molecules (path v).²⁸ Recently, Rimer et al. have thoroughly investigated the crystallization process of silicalite-1 and the dual mechanisms of classical and non-classical crystallization have been demonstrated during the whole process using *in situ* AFM.²⁷ However, *in situ* data are relatively difficult to obtain for directly tracking the changes of structure and morphology because of the rigorous environments and long duration for crystallization,²⁶ therefore, much valuable information for crystallization mechanism has been acquired by some *ex situ* characterizations.^{23,25,26,41} For instance, Subotić et al. and Rimer et al. have investigated the aggregative growth of zeolites ZSM-5,²³ LTL²⁵ and SSZ-13,²⁶ and the crystal morphology and size of SSZ-13 could be changed with the addition of organic modifiers.²⁶

Scheme 1. Possible pathways of zeolite crystallization.



MTW Zeolite possesses a 1D channel system composed of parallel 12-membered ring (12-MR) micropores along the *b* [010] direction.⁴² However, the 1D channelled zeolite always tends to form anisotropic crystal with the longest axis along the orientation of its channels, so that the morphology and size of MTW crystals are of critical importance for their adsorption and catalytic applications.^{43,44} Generically, MTW zeolite can be synthesized with several organic structure directing agents (OSDAs), and the product morphologies are related to the kind of OSDAs.⁴⁵⁻⁴⁸ Among these OSDAs, tetraethylammonium hydroxide (TEAOH) is commercial and the most widely used for the synthesis. Recently, effects of different parameters such as Si source, Al source, alkalinity, Si/Al ratio, H₂O/SiO₂ ratio and so on are carefully studied using this OSDA to control the size and morphology of MTW zeolite.²² The comprehensive understanding of the formation mechanism is significant for more scientifically regulating its morphology. To the best of our knowledge, the crystallization mechanism of MTW zeolite is still equivocal.

In this study, MTW zeolite mesocrystals with morphologies from loosely-attached nanocrystallite assembly to that one with relative dense structure have been obtained by deliberately changing H₂O/SiO₂ ratio to adjust the crystallization kinetics. The crystallization processes of typical products have been systematically investigated by monitoring the whole evolution process using X-ray diffraction (XRD), scanning electron microscopy (SEM), transmission electron microscopy (TEM), inductively coupled plasma-atomic emission spectrometry (ICP-AES), Raman spectra,²⁷ Al magic angle spinning nuclear magnetic resonance (²⁷Al MAS NMR)

and dynamic light scattering (DLS). Furthermore, two typical probe reactions of cumene cracking and 1,2,4-trimethylbenzene (TMB) transformation are carried out not only to explore the detailed catalytic performance and possible application but also to further confirm the effectivity of this method for tailoring the crystal morphology.

2. EXPERIMENTAL SECTION

Materials. TEOAH (25wt%, aqueous solution), silica sol (LUDOX HS-40, 40wt%, aqueous solution), cumene (GC) and 1,2,4-TMB (AR) were purchased from Sigma-Aldrich. Sodium aluminate (54wt% Na₂O, 41wt% Al₂O₃, 5wt% H₂O) and ammonium nitrate (NH₄NO₃) were purchased from Sinopharm Chemical Reagents Co., LTD. All chemicals were used as received without any purification.

Preparation of zeolite MTW. Zeolite samples were synthesized in the systems of 0.0173Na₂O: 0.0083Al₂O₃: 0.16TEAOH: SiO₂: xH₂O, where x = 5-40. The resulted samples are denoted as MTW-x-t, where x is H₂O/SiO₂ ratio and t is the heating time. Typically, 7.09 g of TEOAH solution was added as OSDA into 1.44 g of H₂O in a bottle under stirring for 10 min and then 0.15 g of NaAlO₂ was added into the system under stirring until the NaAlO₂ has been completely dissolved. Next, 11.31 g of silica sol solution was added dropwise. Afterwards, the clear solution after agitation for 3 h at room temperature was transferred into a Teflon-lined autoclave, and then the autoclave was sealed and heated at 160 °C under static condition for 120 h. The resulted products were collected by filtering with filter paper, washing with deionized water and drying at 80 °C. Finally, the products were calcined at 550 °C for 6 h in air to remove OSDA. Similar procedures are used for the samples of x = 20-40 but with more amount of water added in TEOAH, while for that with x = 5, the excessive water was evaporated at 80 °C. The products separated by filtration are denoted as MTW-x-12of. For studying the crystallization mechanism, some products were extracted at predetermined crystallization time. For the intermediate products, we adopted the centrifugation to separate the solid and liquid phases. The typical samples for catalytic reactions were ion exchanged by NH₄NO₃ solution at 80 °C for three times followed by a calcination step at 550 °C for 6 h.

Materials characterization. XRD patterns of the products were recorded on a Bruker D8-Advanced diffractometer (Cu-K_α, 40 kV, 40 mA). SEM images were obtained on Hitachi S-4800 operated at 10 kV within a 1.5 mm working distance. TEM experiments were performed on JEOL JEM-2011 and Tecnai G2 F20 S-Twin operated at a voltage of 200 kV. Fast Fourier transform (FFT) images were obtained from the selected areas using DigitalMicrograph software. The ultrathin cross sections with a thickness of 70-80 nm were prepared on a UC-7 (Leica, Germany) ultra-microtome by using a DIATOME 45° diamond knife at cutting speed of 0.5 mm s⁻¹. Atomic force microscopy (AFM) images of products were obtained in tapping mode on Dimension ICON controller (Bruker Instruments) with sharp silicon cantilever probes (OTESPA, Bruker). The N₂-sorption experiments were conducted on a Quantachrome autosorb iQ-2 instrument at 77 K. Raman spectra were obtained from a Horiba Jobin Yvon XploRA confocal microscope with a 532 nm laser. ²⁷Al MAS NMR was determined on Bruker DSX 300 spectrometer. DLS

was measured on a Nano-ZS90 zetasizer. The particle size distribution was measured for the products after three kinds of separation methods: without centrifugation, with low speed centrifugation (LSC, 10000 rpm for 3 min with a relative centrifugal force of 10277 g), and with high speed centrifugation (HSC, 15000 rpm for 60 min with a relative centrifugal force of 19118 g). The samples were dispersed and ultrasonically treated in deionized water with concentrations about 0.2 wt%. The supernatant liquids separated from the mixture after LSC or HSC were analyzed by ICP-AES for detecting the concentration changes of species in the system. All the supernatant liquids were diluted 100 times prior to analysis. The chemical compositions of final products were determined by X-ray fluorescence (XRF) with a Bruker AXS spectrometer. The acidities of typical samples were obtained by NH_3 -temperature programmed desorption (NH_3 -TPD) experiment on Micromeritics AutoChem II 2920.

Catalytic experiments. Cumene cracking was conducted in a micro-fixed bed reactor by pulse injection with 1 μl every time. The reaction condition was 300 $^\circ\text{C}$ under atmosphere pressure. 0.03 g of catalyst (20-40 mesh) was pre-heated at 450 $^\circ\text{C}$ for 1 h prior to cumene cracking under a He carrier flowing at 40 ml min^{-1} . The products were analyzed by an on-line gas chromatograph (GC) equipped with a thermal conductivity detector (TCD) and packed column (PEG-20M). Transformation of 1,2,4-trimethylbenzene was conducted in a continuous fixed-bed reactor under atmospheric pressure. The weight hourly space velocity (WHSV) was 0.5 h^{-1} and reaction temperature was 300 $^\circ\text{C}$. Prior to the reaction, all the catalysts were activated in N_2 atmosphere at 300 $^\circ\text{C}$ for 2 h. Moreover, the products were analyzed per 40 min using an online GC equipped with a flame ionization detector (FID) and high-resolution capillary column (HP-INNOWAX).

3. RESULTS AND DISCUSSION

3.1 Synthesis of MTW zeolites with diverse morphologies.

A series of zeolite products are synthesized under different $\text{H}_2\text{O}/\text{SiO}_2$ ratios from 5 to 40 at 160 $^\circ\text{C}$ for 120 h using TEAOH as OSDA. XRD patterns (Figures 1A and S1A) show that the pure MTW phase with high crystallinity can be synthesized under $\text{H}_2\text{O}/\text{SiO}_2$ ratios of 10–30. Once that is lower than 10, BEA with impurity of MTW (\star) is mainly produced (Figure 1A-a); while MFI phase with a few of MTW (\star) is mainly obtained as $\text{H}_2\text{O}/\text{SiO}_2$ larger than 30 (Figure 1A-e). The porosities of three pure phase MTW zeolites are characterized by N_2 -sorption experiment. Their isotherms (Figure 1B) combining both I and IV types indicate the coexistence of micro- and mesopores. The uptake of isotherms at high relative pressure (P/P_0) increases when lowering $\text{H}_2\text{O}/\text{SiO}_2$ ratio, implying the gradual enrichment of mesoporosity. The mesopore size distributions estimated by BJH method (inset, Figure 1B) show that MTW-10-12of contains rich mesopores, while no obvious mesopore is detected in MTW-30-12of except a pseudo-peak at 3.8 nm, indicating its relatively dense structure. The detailed data on V_{meso} and S_{ext} (Table S1) also confirm this result. They decrease from 0.311 to 0.133 $\text{cm}^3 \text{g}^{-1}$ (V_{meso}) and from 101 to 62 $\text{m}^2 \text{g}^{-1}$ (S_{ext}), respectively, as $\text{H}_2\text{O}/\text{SiO}_2$ ratio increases from 10 to 30 (Figure 1C). Considering the similar values of S_{BET} and V_{micro} for these samples (Table S1), it suggests that high crystalline MTW zeolite can

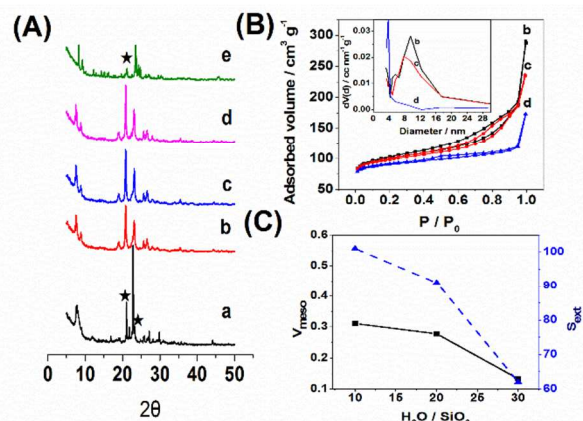


Figure 1. XRD patterns (A), N_2 -sorption isotherms (B), mesopore size distribution (inset) of the samples for MTW-5-12of (a), MTW-10-12of (b), MTW-20-12of (c), MTW-30-12of (d), and MTW-40-12of (e). The changes of V_{meso} and S_{ext} prepared at various $\text{H}_2\text{O}/\text{SiO}_2$ ratios (C).

be facily obtained with tunable mesopores and well-maintained zeolitic micropores.

The product particles of zeolite MTW have the sizes in the range from about 350 to 1000 nm or more with slightly increased mean diameter, from about 600 to 750 nm with the increase of $\text{H}_2\text{O}/\text{SiO}_2$ ratio, as determined by DLS measurements (Figure S1B). As SEM images shown, all of these samples are nanoparticle aggregates (Figure S2), but some differences could be displayed in surface morphology (Figures 2A-C). MTW-10-12of and MTW-20-12of exhibit a rough surface composed of highly-aggregated 20–30 nm nanocrystallites (Figures 2A and 2B), whereas some relatively smooth surfaces could be found for MTW-30-12of (Figure 2C). AFM topographical image further confirms the rough surface of MTW-10-12of with large step heights exceeding 20 nm (Figures 3A and 3C), while the relatively smooth surface of MTW-30-12of could be observed besides rough parts (Figures 3B and 3D). The detailed structures of the samples are identified from

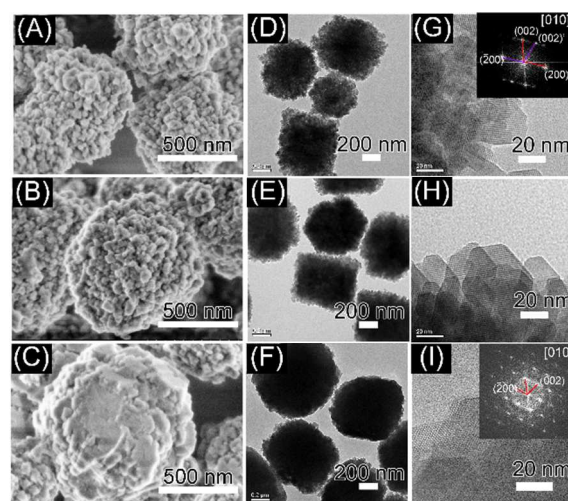


Figure 2. SEM (A-C) and TEM (D-I) images of MTW-10-12of (A, D, G), MTW-20-12of (B, E, H) and MTW-30-12of (C, F, I). The insets of (G, I) are the FFT images.

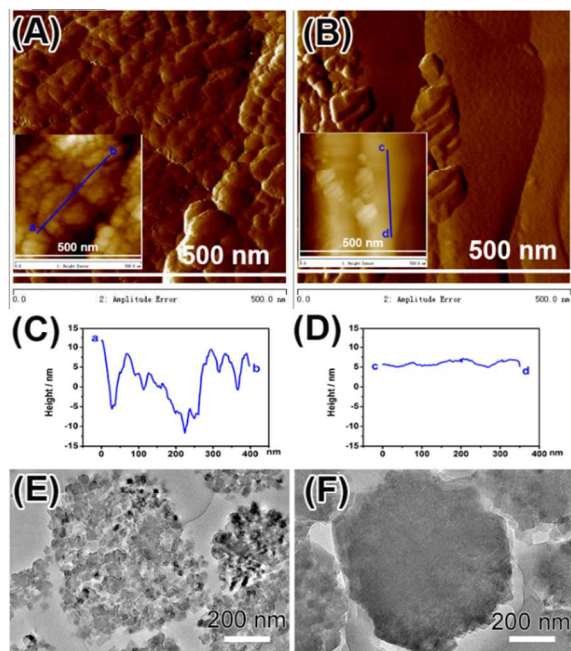


Figure 3. AFM amplitude mode images for MTW-10-12of (A) and MTW-30-12of (B) and their height mode images (insets). (C) and (D) are the section analysis along the lines *ab* and *cd* in the insets of (A) and (B), respectively. The ultrathin specimen TEM images of MTW-10-12of (E) and MTW-30-12of (F).

TEM images. A structure with loosely-aggregated nanocrystallites can be observed in the sample of MTW-10-12of (Figure 2D), which is consistent with its TEM image of ultrathin cross section (Figures 3E and S3A) and N_2 adsorption result with high mesoporosity (Table S1). HRTEM and FFT images present its feature of mesocrystal with b-axis oriented aggregated nanocrystallites of zeolite MTW polymorphs³⁶ (Figures 2G and inset, S3B). However, MTW-30-12of exhibits a denser center as shown in TEM image (Figure 2F), which is further confirmed through ultramicrotomy (Figures 3F and S3C) and N_2 -sorption with relatively lower mesoporosity (Table S1). The single crystal-like diffraction pattern of monoclinic MTW zeolite⁴² is displayed at the edge of particles in HRTEM and FFT images (Figures 2I and inset, S3D). For MTW-20-12of, its particulate properties are at the mid-level (Figures 2E and 2H).

Despite the zeolite MTW mesocrystals are harvested under all of these conditions, some differences on the morphology and porosity could be witnessed, indicating these physical properties can be well controlled by adjusting the H_2O/SiO_2 ratio. The crystallization behaviours of two typical products (MTW-10-t and MTW-30-t) are further investigated in the following sections via comprehensively tracing the evolutions of gel state, particle size, crystallinity, morphology, composition, and framework structure of the intermediate products.

3.2 Investigation on MTW zeolite crystallization.

(1) Crystallization process of MTW-10-t.

The MTW zeolite mesocrystals of loosely-aggregated nanocrystallites with abundant mesopores and rough macrostep

surfaces are harvested as $H_2O/SiO_2 = 10$ (Figures 1, 2 and 3). These phenomena suggest that MTW-10-t is formed probably by nanoparticle self-assembly.⁴⁹ Such zeolite crystallization via nanoparticle aggregation or attachment has been reported in the previous literatures,^{50,51} and recently is termed as a non-classical pathway.²⁴⁻²⁶

DLS results of the whole products without centrifugation display a peak during the crystallization process, and a jump is found from about 80 to 550 nm when the heating time is prolonged from 26 to 27 h (Figure S4A). Two different speed of centrifugations (LSC and HSC) are further employed to separate the products, and the corresponding results of photograph and DLS are shown in Figures S5 and S6, respectively. Almost the same phenomena are observed after LSC and HSC for photographs and DLS. The nanoparticles in the initial clear solution quickly aggregate into bulk network of hydrogel after heating for 6-24 h from its photographs (Figure S5A), which could present as small worm-like aggregated nanoparticles (WLPs) after ultrasound pretreatments for DLS (Figure S4A) and SEM/TEM (Figures S7A and S7B) experiments. As prolonging the crystallization time over 26 h, the hydrogel could shrink and collapse, and then rapidly transfer to large particles accompanied by the emergence of liquid phase (Figures S5A and S6A). After 27 h, only one peak with the size about 550-600 nm in DLS are exhibited for the products after both LSC and HSC, and little difference between them is observed from photographs. The crystallinity of obtained solid is determined by XRD, which displays an induction period of about 26 h for MTW-10-t crystallization (Figure S4B). Interestingly, the particle size of MTW-10-28 is similar to that of the final product, but its crystallinity at this time is much lower than that of the latter, indicating that crystallization of the sample mainly takes place after the formation of larger particles.

Electron microscopes (EM) are applied to visually track the morphological evolutions of intermediates. After hydrothermal treatment for 26 h, plenty of amorphous small WLPs collapsed from hydrogel can be observed (Figures 4A and S8), and TEM images show that these WLPs are composed of several 20 nm nanoparticles (Figures S8C and S8D). This is consistent with the results of recent studies of ZSM-5 crystallization.^{23,52} Besides, a very few of aggregated particles

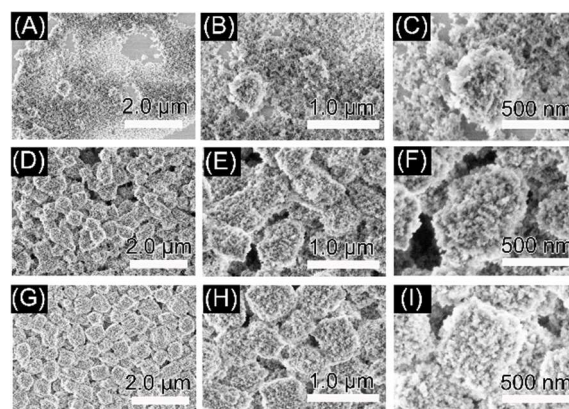


Figure 4. SEM images of products MTW-10-t crystallized with different hydrothermal treatment time, where t is 26 (A-C); 27 (D-F) and 28 h (G-I).

with relatively larger size can be found (Figures 4B and 4C). In the next 2 h, large aggregated particles with the size similar to that of final product are fast formed via nanoparticle aggregation (Figures 4D-I), and their diameter fiercely increases even faster than the crystallinity (Figures S4A and S4B b-d). TEM characterization further confirms the fast aggregation of nanoparticles for the formation of zeolite MTW. Few aggregates with partially crystalline nanoparticles can be discovered in MTW-10-26 (Figures 5A, 5B and inset). At prolonged hydrothermal treatment ($t = 27$ h), the size of aggregated particles obviously increases via aggregation of nanoparticles (Figures 5C, 5D and inset). After heating for another 1 h (MTW-10-28), larger regular particles with the mean size *ca.* 600 nm are formed (Figures 5E, S9A and S9B). However, the edge of each aggregated particle is much looser and some amorphous nanoparticles still exist (Figure 5F and inset), implying that the crystallization is not complete. It is consistent with the result of XRD. These results indicate that the aggregation of small nanoparticles mainly occurs from 26 to 28 h with a certain extent of crystallization. Prolonging the heating time to 32 even 48 h, the size of as-prepared products has a slight change but the crystallinity rises greatly with clear lattice fringes (Figures S4A, S4B, S9C and S9D). Finally, an aggregated MTW zeolite mesocrystal is formed with a little shrinkage of particle size and a very slight increase of crystallinity.

The compositions of supernatant liquid separated by centrifugations at different speeds are analyzed using ICP-AES (Figure S10). The concentrations of Si and Al components exhibit the same tendency of significant decrease under both LSC and HSC conditions. Their concentrations in the initial clear solution are as high as 107.8 (Si) and 2.1 (Al) g L^{-1} (Figure S10, red dot). These values drop to only 49.1 and 0.6 g L^{-1} at 27 h after LSC and 42.8 and 0.2 g L^{-1} after HSC, respectively (Figure S10). With prolonging the heating time, the nutrients concentrations in the supernatant liquid are similar for these two different speed centrifugations. At 28 h, the concentrations of Si and Al decrease to *ca.* 35.0 and 0.5 g L^{-1} respectively, which are about 32% and 23% of their initial concentrations (Figures S10A-d and 10B-d). It indicates that

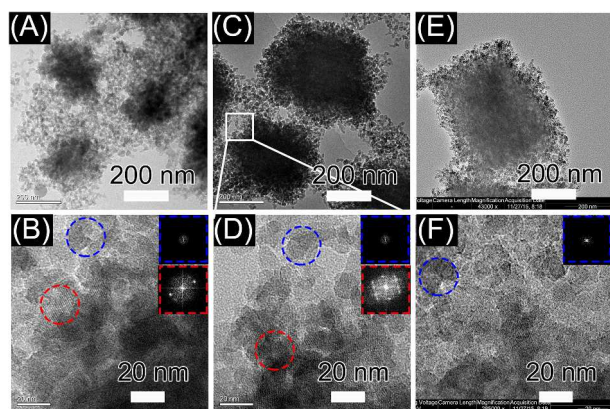


Figure 5. TEM images and HRTEM images of products MTW-10-*t* crystallized with different hydrothermal treatment time, where *t* is 26 (A, B); 27 (C, D) and 28 h (E, F). The blue and red cycles display the typical amorphous and crystalline regions, respectively. The insets are the FFT images of the corresponding regions.

much of nutrition in the liquid has been transferred into the solid phase by nanoparticle aggregation at this time. Subsequently, the concentration of Si slightly decreases to *ca.* 20.0 (19%, 40 h) and 16.8 g L^{-1} (16%, 48 h), which might be due to the somewhat Ostwald ripening in the final stage of crystallization. Meanwhile, the changes of solid productivity (m_t/m_0) during the whole crystallization process are also tracked (Figure S10C), where m_t is the mass of extracted products after LSC at predetermined heating time (*t*), and m_0 is the total contents of Si and Al added into the system at the beginning. It is clear that the productivity is *ca.* 64% after 27 h (Figure S10C) and the value increases to about 75% after further crystallization to 28 h. In consideration of the final solid productivity (85%), it implies that majority of nutrition has been fixed in the solid phase at this time, which is in accordance with the results of ICP-AES.

Raman spectroscopy is an excellent technique to characterize the short-range order of zeolite.⁵³ After heating for 24 h, there is no obvious band for MTW zeolite, indicating the absence of short-range order (Figure S11-a). During the crystallization period, the short-range order can be observed with distinct bands at 370, 400 and 800 cm^{-1} (Figure S11), which are ascribed to ν_s (Si-O-Si) symmetry vibration.^{54,55} It is noted that the intensities of bands at 28 h are almost the same to the final products (Figure S11-d), although the crystallinity is considerably low (Figure S4B-d). It suggests that the short-range order has been mostly built up at this time, similar to the observations in other zeolites.²⁰ Figure S12 is the ²⁷Al MAS NMR of the samples, in which only a signal is found at *ca.* 50-55 ppm corresponding to tetrahedrally coordinated aluminium atoms in the framework.⁵⁶ Moreover, this signal gradually becomes narrow (Figure S12B), reflecting the improvement in the homogeneity of framework aluminium atoms.⁵⁷ The above results indicate that MTW-10-*t* is formed mainly via fast aggregation of nanoparticles followed by an internal reorganization.

(2) Crystallization process of MTW-30-*t*.

MTW-30-*t* presents some different behaviors in its crystallization process comparing with MTW-10-*t*. Bi-modal distribution of particle size is witnessed for whole products in DLS results after heating for 54 h (Figure S4C). In order to distinguish the particles with different size in the products, LSC and HSC are adopted for the separation. If the centrifugation is conducted at a high speed, two peaks can be observed (Figure S6D), similar to that of the whole products (Figure S4C). However, only one peak corresponding to the larger particles is exhibited after LSC (Figure S6C). These phenomena certify the existence of small nanoparticles of about 100 nm during the crystallization process. Photographs of different centrifugation conditions can visually present this fact (Figure S5B). Comparing with LSC, a much clearer supernatant liquid can be obtained if the samples are separated by HSC, implying the presence of small nanoparticles in the solution. Thus, a two-step centrifugation method is adopted to collect the small nanoparticles, and TEM images as well as XRD result confirm that they are amorphous WLPs (Figure S13). To conveniently gain insight into its crystallization process, the solid products obtained by LSC are further characterized for eliminating the interference of small WLPs. XRD patterns display that the crystallization rate of MTW-30-*t* is

obviously slower than that of MTW-10-t. Its induction period prolongs to *ca.* 54 h (Figure S4D). This is because that the lower concentrations of nutrients and alkalinity in reaction system could decelerate its crystallization.⁵⁸

The crystallization process of MTW-30-t is further detailed by other characterizations. As shown in Figure S5B, the sol becomes more and more turbid from 0 to 48 h but no solid phase can be separated by LSC. Through directly observing the sol with SEM, the primary nanoparticles in the initial solution gradually aggregate into small WLPs with a slight increased size during 12–48 h (Figure S14), in agreement with DLS results (Figure S4C). As such, the concentrations of Si and Al components in the sol vary gently in the first 48 h after LSC (Figures S15A and S15B), but their concentrations decrease dramatically after HSC (Figures S15D and S15E) due to the separation of small WLPs from supernatant liquid under this condition (Figure S5B). When the heating time is prolonged to 54 h, plenty of precipitates are formed and can be collected even at LSC, so that the m_t/m_0 is *ca.* 80%. The concentrations of nutrition in the supernatant liquid after LSC decrease to the value (Figures S15A and S15B b) even similar to those after HSC (Figures S15D and S15E b). DLS experiment shows the particle size in solid is *ca.* 180 nm (Figure S4C-b), and SEM images (Figures 6AI and S16A) indicate that these obtained precipitates virtually are small aggregated WLPs formed by chain aggregation of primary nanoparticles.⁵² In addition, there are very few particles of about 300 nm with some relatively smooth terraces (Figure 6AII) in the product. And TEM images show that they are crystalline with relatively denser structure (Figures 7A and 7B), which are different from loose structure of MTW-10-t (Figures 5A and 5B). It might be because that a slower rate of crystallization in such a dilute system causes the easier fusion of aggregated WLPs.

It is surprising that m_t/m_0 value decreases accompanied with the increase of particle size and crystallinity from 54 to 72 h (Figures S15C, S4C and S4D b-e), and the concentrations of Si and Al components rapidly increase in supernatant liquid correspondingly after LSC (Figures S15A and S15B b-e). However, after HSC in which both small and large particles could be removed, the concentrations of nutrition in the supernatant liquid still keep low values (Figures S15D and S15E b-e). It indicates that the pre-formed precipitates at 54 h could gradually disaggregate into smaller sized WLPs referring to DLS results, in which the peak corresponding to relatively small nanoparticles reappears (Figure S4C). Moreover, a tiny rebound could also be tracked after HSC, probably due to the generation of some simple species during this stage. After 72 h, the concentrations of nutrition in supernatant liquid reach to a low value after HSC with slight changes afterwards (Figures S15D and S15E e-g), while their concentrations after LSC decrease consecutively (Figures S15A and S15B e-g). Correspondingly, the solid productivity (m_t/m_0) increases accompanied with a little improvement of crystallinity (Figures S4D and S15C e-g), suggesting the migration of nutrients from liquid to solid.

SEM/TEM and DLS experiments are applied to further monitoring of the evolution of zeolite crystals after 54 h. The sample obtained before 54 h mainly exists as amorphous WLPs. However, at crystallization of 60 h, the zeolite crystals

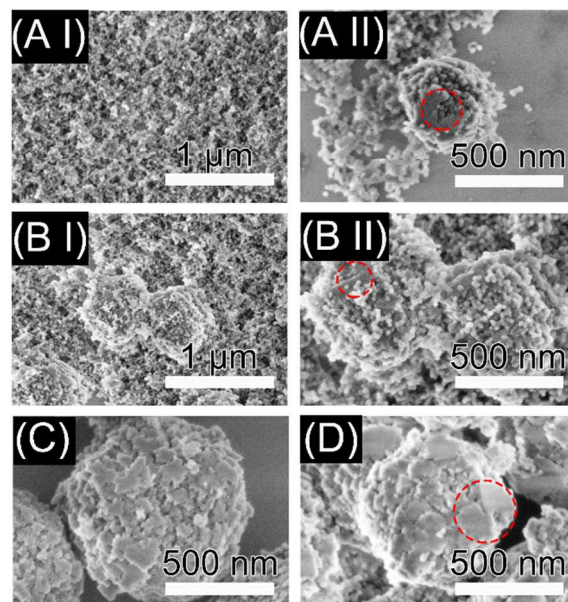


Figure 6. SEM images of MTW-30-t crystallized with different hydrothermal treatment time, where *t* is 54 (A), 60 (B), 72 (C) and 96 h (D). The red circles display the relatively smooth terraces.

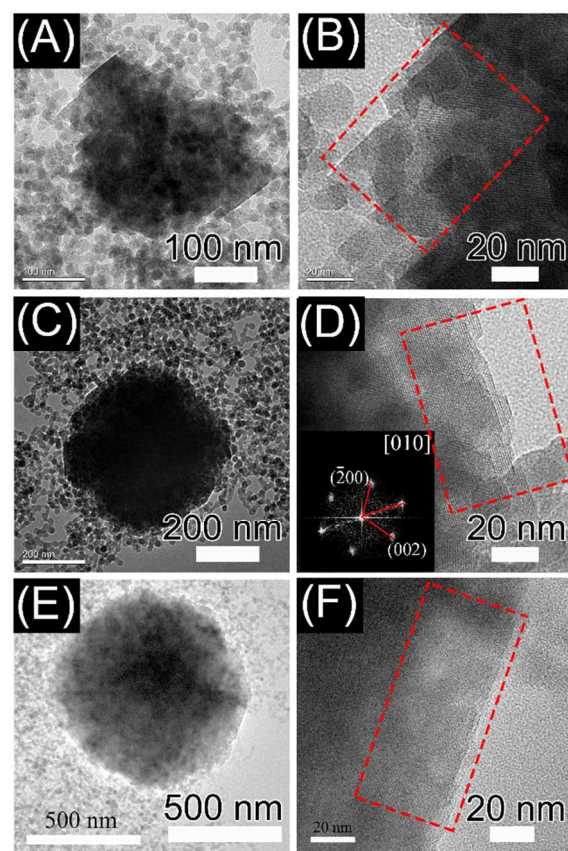
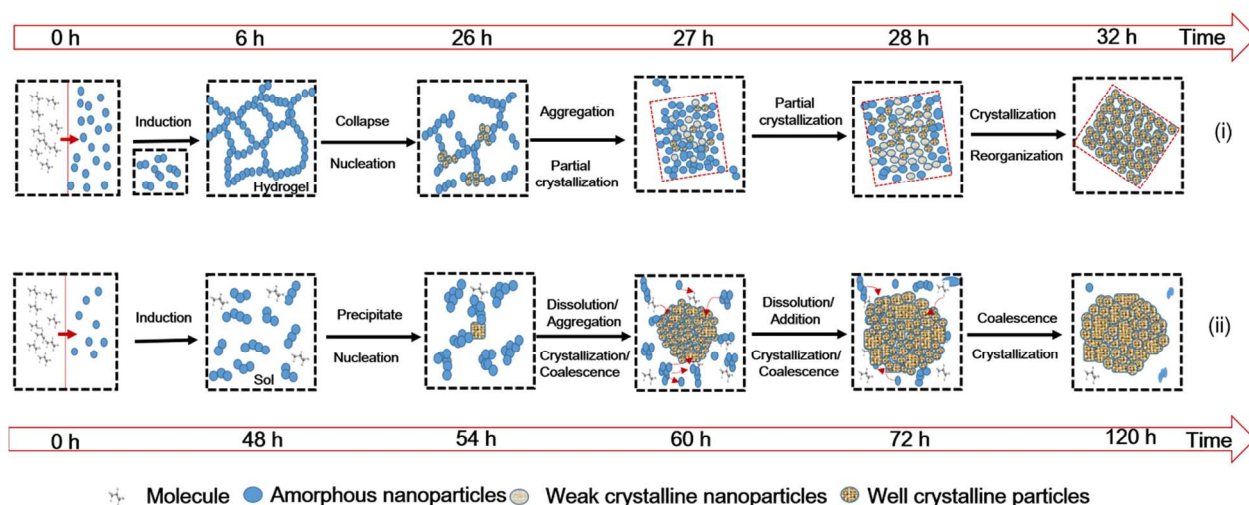


Figure 7. Representative TEM images of MTW-30-t crystallized with different hydrothermal treatment time, where *t* is 54 (A, B), 60 (C, D) and 66 h (E, F). The inset of (D) is the FFT image and the red rectangles display a relatively complete lattice.

Scheme 2. Crystallization pathways of MTW zeolite: MTW-10-t (i) and MTW-30-t (ii).



could be easily observed with nanoparticle aggregated morphology and some smooth terraces in their SEM images (Figure 6B). The DLS profile shows the obvious peak corresponding to the product particle diameter centered at *ca.* 500 nm (Figure S6C) which is *ca.* 68% of the crystal size of final product (i.e., MTW-10-12of). Their TEM images present a relatively dense structure with continuous lattice fringes at the edge of the particles (Figures 7C and 7D), and a single crystal-like pattern of monoclinic MTW zeolite can be observed from FFT image (inset, Figure 7D). These results indicate that the coalescence of the participating WLPs happens accompanied with their aggregation during crystallization process, probably intertwined with the addition of simple species. Afterwards, the mean particle size of zeolite crystal continuously increases to *ca.* 730 nm as prolonging the heating time over 60 h (Figure S6C). Meanwhile, the smooth terraces are more obvious from the SEM images (Figures 6C, 6D, S16B and S16C) and their TEM images show the crystal quality is more perfect with the continuous lattice fringes observed from the edge of the crystal (Figures 7E and 7F). These results imply that the co-occurrence of addition and merging of WLPs/simple species during crystal growth process. As a result, a dense crystalline MTW zeolite with some smooth terraces is obtained (Figures 6C, and 2C).

The intermediate solid products of MTW-30-t are also characterized by Raman spectroscopy and ^{27}Al MAS NMR. When precipitates produce from sol solution at 54 h, Raman spectrum has shown some weak peaks corresponding to the short-range order of MTW framework (Figure S17A-b) with appearance of weak peaks in XRD pattern (Figure S4D-b), indicating the formation of a few crystalline nuclei. Subsequently, the intensity of Raman peaks for zeolite continuously improve accompanied with the increase of crystallinity and particle size. Meanwhile, the gradual improvement of zeolite framework quality is also reflected from the narrowing of the signal for tetrahedrally coordinated aluminium atoms in ^{27}Al MAS NMR (Figure S17B) with prolonging the crystallization time.

3.3 Crystallization mechanism of MTW zeolite.

The above experimental results show that MTW zeolites follow the similar particle aggregation and crystallization processes under different $\text{H}_2\text{O}/\text{SiO}_2$ ratios but with some different behaviors. It can be summarized in Scheme 2.

The crystallization of MTW-10-t takes place by a chain of events, shown as Path i in Scheme 2: (1) The formation of precursor particles with size about 20 nm after aging for 3 h (as determined by DLS, Figure S18), and after heating for 1 h they aggregate into WLPs with size *ca.* 40 nm. (2) The formed WLPs aggregate into a loosely-hold hydrogel network after heating for 6-24 h, which will disaggregate into small WLPs at 26 h. (3) Then these WLPs quickly re-aggregate into the large and loose particles with mean size up to about 600 nm (similar to that of final product) at *ca.* 27-28 h, but with low crystallinity. The processes (1) - (3) are consistent with the recently described mechanism of the formation and evolution of WLPs during crystallization of zeolites ZSM-5,²³ LTL²⁵ and SSZ-13.²⁶ (4) The main part of crystallization takes place by internal reorganization from 28 to 32 h. Finally, a high crystalline mesocrystal MTW zeolite is obtained with b-axis oriented-aggregated structure, rough surface and abundant mesoporosity, which are regarded as the indicators of non-classical crystallization mechanism.²⁴⁻²⁷

MTW-30-t prepared in a dilute system also follows the aggregation-crystallization process but with some different features compared with MTW-10-t, summarized as Path ii in Scheme 2: (1) The WLPs are gradually formed with an increasing size via aggregation of nanoparticles in induction period. (2) The WLPs aggregate into larger aggregated precipitates at 54 h rather than hydrogel network due to the considerably smaller specific number of WLPs in this system, and a few of crystalline nuclei are generated at this time. The processes (1) and (2) are consistent with the recently described mechanism of the formation and evolution of WLPs during short-time hydrothermal treatment of dilute TPA-aluminosilicate reaction mixture.⁵² The precipitates could then gradually disaggregate/dissolve into small WLPs or simple species which may act as nutrition in the subsequent crystallization period. (3) The dense zeolite crystal of about 500 nm (*ca.* 68% of final product in diameter) is formed via

co-occurrence of aggregation and coalescence of WLPs in the period of 54-60 h. (4) The size and crystallinity of particles continuously increase via addition and merging of WLPs in the following time, probably accompanied with addition of some simple species. Finally, a product with relatively dense structure and some smooth terraces could be collected.

In a short summary, the crystallization of MTW zeolite follows a series of events including the formation of WLPs, gelation via aggregation of WLPs, and disaggregation of gel (induction period), followed by formation of aggregates accompanied with crystallization (crystallization/growth period). In the induction period, a hydrogel could be generated in a concentrated system via the aggregation of pre-formed WLPs due to the high collision frequency.⁵² With the decrease of nutrients concentrations, the precipitates are formed due to the considerably smaller specific number of WLPs. After gelation, the hydrogel/precipitates can disaggregate into WLPs as the nutrients for the following crystallization process.

In the following crystallization/growth period, it seems that the formation of about 500-600 nm sized aggregates is a critical step for the intense transformation of amorphous to crystalline phase due to higher "concentration" of aluminosilicate materials, which is favorable for the formation of nuclei and their growth.^{23,26} In a concentrated system, an internal reorganization or crystallization process takes place after the fast formation of aggregates to produce a loosely-aggregated zeolite product. With the decrease of nutrition concentrations, the coalescence of the participating WLPs is more notable due to the lower crystallization rate in a dilute system, thus a relatively denser MTW zeolite is obtained. Moreover, the addition of WLPs/simple species could also occur due to a slower rate of aggregation. Therefore, we can facily regulate the textural properties of MTW zeolite products by adjusting the compositions of initial mixtures to control the crystallization kinetics.

3.4 Evaluation of acidity and catalytic performance.

The acidity and catalytic performance of different morphological MTW zeolites are evaluated. As shown in Figure 8A and Table S2, both samples possess almost the same TPD profiles with similar acid site distribution and total amount of acids (MTW-10-12of: 0.428 mmol g⁻¹; MTW-30-12of: 0.412 mmol g⁻¹), which is consistent with their similar Si/Al ratio (Table S1). Cumene cracking is reported as a model reaction to characterize the Brønsted acid sites resulted from framework aluminium in zeolite.⁵⁹ Both samples have very similar catalytic performance for this reaction (Figure S19). At the first dose, the conversions of cumene are 71.5% and 68.4% on MTW-10-12of and MTW-30-12of, respectively, and then both of them present a slowly decreasing trend due to the formation of coke. This result further indicates the similar acidic properties of MTW-10-12of and MTW-30-12of.

The transformation of 1,2,4-trimethylbenzen (1,2,4-TMB) is further applied as a probe reaction to research the relationships between morphology and catalytic property of MTW zeolite for its special reaction network containing

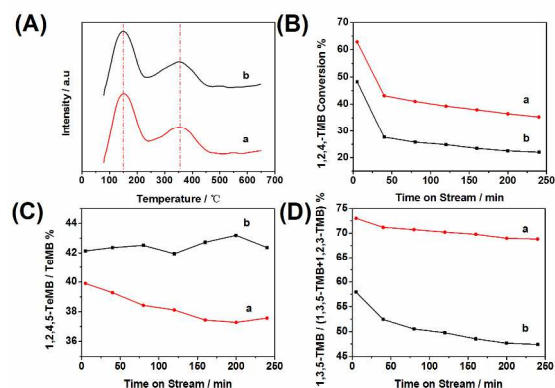
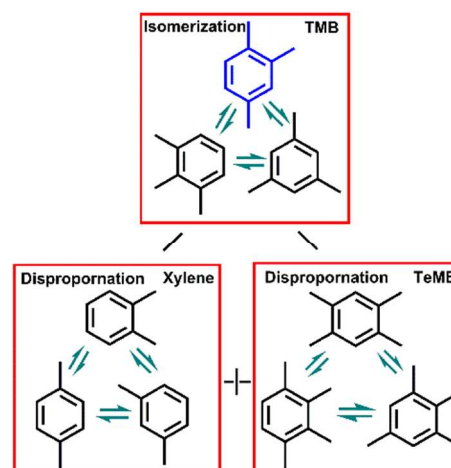


Figure 8. NH₃-TPD profiles, which have been vertically off-setted (A); conversion of 1,2,4-trimethylbenzene (B); the ratio of 1,2,4,5-isomer in TeMB (C); the ratio of 1,3,5-isomer in TMB products (D) of MTW-10-12of (a) and MTW-30-12of (b).

isomerization and disproportionation pathways (Scheme 3).^{60,61} As shown in Figure 8B, the conversions on both catalysts decay quickly in the first 40 min followed by a slowly declining trend. However, the conversion on MTW-10-12of is always higher than that of MTW-30-12of during the whole reaction process. Due to the similar acidic property of both samples, the higher conversion of MTW-10-12of is determined by its larger mesoporous volumes and larger external surface areas. Accordingly, the disproportionation/isomerization ratios ($S_{d/i}$) of both samples also drop down very rapidly in the first 80 min, but the $S_{d/i}$ of MTW-10-12of is always higher than that of MTW-30-12of (Table S3). This phenomenon can be explained by the different mesoporosities of both samples. The disproportionation of 1,2,4-TMB occurs via a bimolecular mechanism, which produces a bulky biphenylmethane carbocation intermediate.^{60,61} Therefore, MTW-10-t with open structure shows a relative higher $S_{d/i}$ value. With prolonging the reaction time, the selectivity of disproportionation decays rapidly while that of isomerization increases. It is attributed to the heavier influence of coking on the disproportionation with bimolecular route.⁶¹

Scheme 3. Disproportionation and isomerization of 1,2,4-TMB.



The different porosities of these samples can be further reflected by the product distributions of 1,2,4-TMB transformation. Both samples yield the xylene isomers in the similar ratio of thermodynamic equilibrium due to the smaller sizes of these molecules (Table S3). However, for tetramethylbenzene (TeMB), another kind of disproportionation products, a very different behaviour is observed (Figure 8C). For MTW-10-12of, 1,2,4,5-TeMB with a relative smaller kinetic diameter presents a lower ratio in all of TeMB products than on MTW-30-12of. As have been reported in literatures,^{62,63} amongst all TeMB isomers, 1,2,4,5-TeMB could be generated in the micropore channel of zeolite for its smaller size and then it would isomerize consecutively into its isomers with relative larger size on the external surface or mesopores, such as 1,2,3,4- or 1,2,3,5-TeMB. Due to the enhanced mesoporosity of MTW-10-12of, isomerization of TeMB would take place easier on its enriched external surface, leading to the lower ratio of 1,2,4,5-TeMB. A different trend is observed on the distribution of trimethylbenzene (TMB) isomers (Figure 8D). MTW-10-12of displays a higher 1,3,5-TMB ratio than MTW-30-12of. It can also be explained by the different mesoporosities of these samples. Due to the larger size of 1,3,5-TMB, it mainly yields from reactant of 1,2,4-TMB on the external surface or in mesopores.^{62,63} The open structure of MTW-10-12of benefits its generation. The same phenomenon has been reported on NU-87 with similar micropore size.⁶²

4. Conclusions

A series of zeolite MTW mesocrystals with oriented nanocrystallites and morphologies from dense to loose structures are obtained just by deliberately regulating the crystallization kinetics. The crystallization of MTW zeolite follows the intertwined classical/non-classical mechanism under different H₂O/SiO₂ ratios, including the formation of WLPs, aggregation of WLPs and crystallization of aggregates. The formation of about 500-600 nm sized aggregates is a critical step for the intense transformation of amorphous to crystalline phase. Remarkably, some different features in crystallization processes could be found under concentrated and dilute systems. The b-axis oriented nanocrystallite-aggregated MTW zeolite with abundant mesopores and rough surfaces is obtained under the condition of concentrated solution (H₂O/SiO₂ = 10), which is formed by a fast aggregation of WLPs to the size of final product, followed by an internal reorganization process. Nonetheless, in a dilute system (H₂O/SiO₂ = 30), the aggregates with the size smaller than the final product (< 70%) are firstly observed via aggregation/coalescence of WLPs accompanied by crystallization. Thereafter, the zeolite crystal continuously grows via addition and coalescence of WLPs, probably with some simple species. As a result, a dense MTW zeolite with some relatively smooth terraces is harvested. Moreover, two typical samples are evaluated through cumene cracking and transformation of 1,2,4-TMB. The conversions and distribution of products with different molecular sizes further confirm the features of zeolites and their effects on catalytic reactions. These results can guide us to simply and effectively design MTW zeolite with different morphologies for meeting the practical demands of various catalytic reactions in the chemical industry. It also sheds light on the facile and economical

synthesis of other zeolites with diverse morphologies/porosities by rationally controlling the kinetics of intertwined classical/non-classical crystallization.

ASSOCIATED CONTENT

Supporting Information. SEM images, TEM images, Photograph, XRD patterns, particle size distribution, ICP-AES, ²⁷Al MAS NMR, Raman spectra, pore size distribution and reaction results of MTW zeolite are included. The Supporting Information is available free of charge via the Internet at <http://pubs.acs.org>.

AUTHOR INFORMATION

Corresponding Author

*(Y.T.) E-mail: yitang@fudan.edu.cn.

*(H.B.Z.) E-mail: zhanghongbin@fudan.edu.cn.

Notes

The authors declare no competing financial interest.

ACKNOWLEDGMENT

The authors express their appreciations to Center for Analysis and Measurement of Fudan University and Department of Macromolecular Science for the help of AFM and ultramicrotomy experiments, respectively. Additionally, the authors sincerely acknowledge to a reviewer for his/her enlightening comments, although he/she is anonymous. This work was supported by National Key Basic Research Program of China (2013CB934101), NSFC (21433002, 21573046, 21473037 and U1463206), China Postdoctoral Science Foundation (2015M580289).

REFERENCES

- (1) Dusselier, M.; Van Wouwe, P.; Dewaele, A.; Jacobs, P. A.; Sels, B. F., GREEN CHEMISTRY. Shape-selective zeolite catalysis for bioplastics production. *Science* **2015**, *349*, 78-80.
- (2) Zhang, R.; Liu, N.; Lei, Z.; Chen, B., Selective Transformation of Various Nitrogen-Containing Exhaust Gases toward N₂ over Zeolite Catalysts. *Chem. Rev.* **2016**, *116*, 3658-3721.
- (3) Valtchev, V.; Majano, G.; Mintova, S.; Pérez-Ramírez, J., Tailored crystalline microporous materials by post-synthesis modification. *Chem. Soc. Rev.* **2013**, *42*, 263-290.
- (4) Smit, B.; Maesen, T. L., Towards a molecular understanding of shape selectivity. *Nature* **2008**, *451*, 671-678.
- (5) Reddy, J. K.; Motokura, K.; Koyama, T.-r.; Miyaji, A.; Baba, T., Effect of morphology and particle size of ZSM-5 on catalytic performance for ethylene conversion and heptane cracking. *J. Catal.* **2012**, *289*, 53-61.
- (6) Zhang, H.; Hu, Z.; Huang, L.; Zhang, H.; Song, K.; Wang, L.; Shi, Z.; Ma, J.; Zhuang, Y.; Shen, W.; Zhang, Y.; Xu, H.; Tang, Y., Dehydration of Glycerol to Acrolein over Hierarchical ZSM-5 Zeolites: Effects of Mesoporosity and Acidity. *ACS Catal.* **2015**, *5*, 2548-2558.
- (7) Larlus, O.; Valtchev, V. P., Crystal morphology control of LTL-type zeolite crystals. *Chem. Mater.* **2004**, *16*, 3381-3389.
- (8) Drews, T. O.; Tsaipatsis, M., Progress in manipulating zeolite morphology and related applications. *Curr. Opin. Colloid Interface Sci.* **2005**, *10*, 233-238.
- (9) Wakihara, T.; Ihara, A.; Inagaki, S.; Tatami, J.; Sato, K.; Komeya, K.; Meguro, T.; Kubota, Y.; Nakahira, A., Top-Down Tuning of Nanosized ZSM-5 Zeolite Catalyst by Bead Milling and Recrystallization. *Cryst. Growth Des.* **2011**, *11*, 5153-5158.

- (10) Tao, Y. S.; Kanoh, H.; Abrams, L.; Kaneko, K., Mesopore-modified zeolites: Preparation, characterization, and applications. *Chem. Rev.* **2006**, *106*, 896-910.
- (11) Pérez-Ramírez, J.; Verboekend, D.; Bonilla, A.; Abelló, S. n., Zeolite Catalysts with Tunable Hierarchy Factor by Pore-Growth Moderators. *Adv. Funct. Mater.* **2009**, *19*, 3972-3979.
- (12) Zhang, B.; Zhang, Y.; Hu, Y.; Shi, Z.; Azhati, A.; Xie, S.; He, H.; Tang, Y., Microexplosion under Microwave Irradiation: A Facile Approach to Create Mesopores in Zeolites. *Chem. Mater.* **2016**, *28*, 2757-2767.
- (13) Choi, M.; Na, K.; Kim, J.; Sakamoto, Y.; Terasaki, O.; Ryoo, R., Stable single-unit-cell nanosheets of zeolite MFI as active and long-lived catalysts. *Nature* **2009**, *461*, 246-249.
- (14) Xu, D.; Ma, Y.; Jing, Z.; Han, L.; Singh, B.; Feng, J.; Shen, X.; Cao, F.; Oleynikov, P.; Sun, H.; Terasaki, O.; Che, S., pi-pi interaction of aromatic groups in amphiphilic molecules directing for single-crystalline mesostructured zeolite nanosheets. *Nat. Commun.* **2014**, *5*, 4262-4271.
- (15) Singh, B. K.; Xu, D.; Han, L.; Ding, J.; Wang, Y.; Che, S., Synthesis of Single-Crystalline Mesoporous ZSM-5 with Three-Dimensional Pores via the Self-Assembly of a Designed Triply Branched Cationic Surfactant. *Chem. Mater.* **2014**, *26*, 7183-7188.
- (16) Kore, R.; Srivastava, R.; Satpati, B., ZSM-5 zeolite nanosheets with improved catalytic activity synthesized using a new class of structure-directing agents. *Chem.-Eur. J.* **2014**, *20*, 11511-11521.
- (17) Lupulescu, A. I.; Rimer, J. D., Tailoring silicalite-1 crystal morphology with molecular modifiers. *Angew. Chem., Int. Ed.* **2012**, *51*, 3345-3349.
- (18) Lupulescu, A. I.; Kumar, M.; Rimer, J. D., A facile strategy to design zeolite L crystals with tunable morphology and surface architecture. *J. Am. Chem. Soc.* **2013**, *135*, 6608-6617.
- (19) Gomez, A. G.; de Silveira, G.; Doan, H.; Cheng, C. H., A facile method to tune zeolite L crystals with low aspect ratio. *Chem. Commun.* **2011**, *47*, 5876-5878.
- (20) Zhang, H.; Zhao, Y.; Zhang, H.; Wang, P.; Shi, Z.; Mao, J.; Zhang, Y.; Tang, Y., Tailoring Zeolite ZSM-5 Crystal Morphology/Porosity through Flexible Utilization of Silicalite-1 Seeds as Templates: Unusual Crystallization Pathways in a Heterogeneous System. *Chem.-Eur. J.* **2016**, *22*, 7141-7151.
- (21) Ding, K.; Corma, A.; Macia-Agullo, J. A.; Hu, J. G.; Kramer, S.; Stair, P. C.; Stucky, G. D., Constructing Hierarchical Porous Zeolites via Kinetic Regulation. *J. Am. Chem. Soc.* **2015**, *137*, 11238-11241.
- (22) Masoumifard, N.; Kaliaguine, S.; Kleitz, F., Synergy between structure direction and alkalinity toward fast crystallization, controlled morphology and high phase purity of ZSM-12 zeolite. *Microporous Mesoporous Mater.* **2016**, *227*, 258-271.
- (23) Ren, N.; Subotić, B.; Bronić, J.; Tang, Y.; Dutour Sikirić, M.; Mišić, T.; Svetličić, V.; Bosnar, S.; Antonić Jelić, T., Unusual Pathway of Crystallization of Zeolite ZSM-5 in a Heterogeneous System: Phenomenology and Starting Considerations. *Chem. Mater.* **2012**, *24*, 1726-1737.
- (24) De Yoreo, J. J.; Gilbert, P. U.; Sommerdijk, N. A.; Penn, R. L.; Whitelam, S.; Joester, D.; Zhang, H.; Rimer, J. D.; Navrotsky, A.; Banfield, J. F.; Wallace, A. F.; Michel, F. M.; Meldrum, F. C.; Colfen, H.; Dove, P. M., CRYSTAL GROWTH. Crystallization by particle attachment in synthetic, biogenic, and geologic environments. *Science* **2015**, *349*, aaa6760.
- (25) Kumar, M.; Li, R.; Rimer, J. D., Assembly and Evolution of Amorphous Precursors in Zeolite L Crystallization. *Chem. Mater.* **2016**, *28*, 1714-1727.
- (26) Kumar, M.; Luo, H.; Roman-Leshkov, Y.; Rimer, J. D., SSZ-13 Crystallization by Particle Attachment and Deterministic Pathways to Crystal Size Control. *J. Am. Chem. Soc.* **2015**, *137*, 13007-13017.
- (27) Lupulescu, A. I.; Rimer, J. D., In Situ Imaging of Silicalite-1 Surface Growth Reveals the Mechanism of Crystallization. *Science* **2014**, *344*, 729-732.
- (28) Zheng, J.; Zhang, W.; Liu, Z.; Huo, Q.; Zhu, K.; Zhou, X.; Yuan, W., Unraveling the non-classic crystallization of SAPO-34 in a dry gel system towards controlling meso-structure with the assistance of growth inhibitor: Growth mechanism, hierarchical structure control and catalytic properties. *Microporous Mesoporous Mater.* **2016**, *225*, 74-87.
- (29) Cundy, C. S.; Cox, P. A., The Hydrothermal Synthesis of Zeolites: Precursors, Intermediates and Reaction Mechanisms: Review Article. *Microporous Mesoporous Mater.* **2005**, *82*, 1-78.
- (30) Serrano, D. P.; Escola, J. M.; Pizarro, P., Synthesis Strategies in the Search for Hierarchical Zeolites. *Chem. Soc. Rev.* **2013**, *42*, 9571-9574.
- (31) Kirschhock, C. E. A.; Ravishankar, R.; Jacobs, P. A.; Martens, J. A., Aggregation Mechanism of Nanoslabs with Zeolite MFI-Type Structure. *J. Phys. Chem. B* **1999**, *103*, 11021-11027.
- (32) Davis, T. M.; Drews, T. O.; Ramanan, M.; He, C.; Dong, J.; Schnablegger, H.; Katsoulakis, M. A.; Kokkoli, E.; McCormick, A. V.; Penn, R. L.; Tsapatsis, M., Mechanistic Principles of Nanoparticle Evolution to Zeolite Crystals. *Nature Mater.* **2006**, *5*, 400-408.
- (33) Song, R. Q.; Colfen, H., Mesocrystals--ordered nanoparticle superstructures. *Adv. Mater.* **2010**, *22*, 1301-1330.
- (34) Niederberger, M.; Colfen, H., Oriented attachment and mesocrystals: non-classical crystallization mechanisms based on nanoparticle assembly. *Phys. Chem. Chem. Phys.* **2006**, *8*, 3271-3287.
- (35) Ge, J.; Hu, Y.; Biasini, M.; Beyermann, W. P.; Yin, Y., Superparamagnetic magnetite colloidal nanocrystal clusters. *Angew. Chem., Int. Ed.* **2007**, *46*, 4342-4345.
- (36) He, G.; Dahl, T.; Veis, A.; George, A., Nucleation of apatite crystals in vitro by self-assembled dentin matrix protein 1. *Nat. Mater.* **2003**, *2*, 552-558.
- (37) Fang, Y. M.; Hu, H. Q.; Chen, G. H., In situ assembly of zeolite nanocrystals into mesoporous aggregate with single-crystal-like morphology without secondary template. *Chem. Mater.* **2008**, *20*, 1670-1672.
- (38) Zhang, H.; Ma, Y.; Song, K.; Zhang, Y.; Tang, Y., Nanocrystallite oriented self-assembled ZSM-5 zeolite and its LDPE cracking properties: Effects of accessibility and strength of acid sites. *J. Catal.* **2013**, *302*, 115-125.
- (39) Jacobsen, C. J. H.; Madsen, C.; Houzvicka, J.; Schmidt, I.; Carlsson, A., Mesoporous zeolite single crystals. *J. Am. Chem. Soc.* **2000**, *122*, 7116-7117.
- (40) De Moor, P.-P. E. A.; Beelen, T. P. M.; Komanshek, B. U.; Beck, L. W.; Wagner, P.; Davis, M. E.; van Santen, R. A., Imaging the Assembly process of the Organic-Mediated Synthesis of Zeolite. *Chem. Eur. J.* **1999**, *5*, 2083-2088.
- (41) Kosanovic, C.; Havenscak, K.; Subotic, B.; Svetlicic, V.; Mistic, T.; Cziraki, A.; Huhn, G., A Contribution to Understanding the Mechanism of Crystallization of Silicalite-1 in Heterogeneous Systems (Hydrogels). *Microporous Mesoporous Mater.* **2009**, *123*, 150-159.
- (42) Ritsch, S.; Ohnishi, N.; Ohsuna, T.; Hiraga, K.; Terasaki, O.; Kubota, Y.; Sugi, Y., High-resolution electron microscopy study of ZSM-12 (MTW). *Chem. Mater.* **1998**, *10*, 3958-3965.
- (43) Mehla, S.; Krishnamurthy, K. R.; Viswanathan, B.; John, M.; Niwate, Y.; Kishore Kumar, S. A.; Pai, S. M.; Newalkar, B. L., n-Hexadecane hydroisomerization over

BTMACl/TEABr/MTEABr templated ZSM-12. *Microporous Mesoporous Mater.* **2013**, *177*, 120-126.

(44) Zhang, H.; Zhang, H.; Wang, P.; Zhao, Y.; Shi, Z.; Zhang, Y.; Tang, Y., Organic template-free synthesis of zeolite mordenite nanocrystals through exotic seed-assisted conversion. *RSC Adv.* **2016**, *6*, 47623-47631.

(45) Kamimura, Y.; Iyoki, K.; Elangovan, S. P.; Itabashi, K.; Shimojima, A.; Okubo, T., OSDA-free synthesis of MTW-type zeolite from sodium aluminosilicate gels with zeolite beta seeds. *Microporous Mesoporous Mater.* **2012**, *163*, 282-290.

(46) Li, J.; Lou, L.-L.; Xu, C.; Liu, S., Synthesis, characterization of Al-rich ZSM-12 zeolite and their catalytic performance in liquid-phase tert-butylation of phenol. *Catal. Commun.* **2014**, *50*, 97-100.

(47) Kore, R.; Srivastava, R., Synthesis of zeolite Beta, MFI, and MTW using imidazole, piperidine, and pyridine based quaternary ammonium salts as structure directing agents. *RSC Adv.* **2012**, *2*, 10072-10084.

(48) Ernst, S.; Jacobs, P. A.; Martens, J. A.; Weitkamp, J., Synthesis of Zeolite Zsm-12 in the System (Mtea)₂₀-Na₂O-SiO₂-Al₂O₃-H₂O. *Zeolites* **1987**, *7*, 458-462.

(49) Niederberger, M.; Cölfen, H., Oriented attachment and mesocrystals: Non-classical crystallization mechanisms based on nanoparticle assembly. *Phys. Chem. Chem. Phys.* **2006**, *8*, 3271-3287.

(50) Nikolakis, V.; Kokkoli, E.; Tirrell, M.; Tsapatsis, M.; Vlachos, D. G., Zeolite growth by addition of subcolloidal particles: modeling and experimental validation. *Chem. Mater.* **2000**, *12*, 845-853.

(51) Kumar, S.; Davis, T. M.; Ramanan, H.; Penn, R. L.; Tsapatsis, M., Aggregative growth of silicalite-1. *J. Phys. Chem. B* **2007**, *11*, 3398-3403.

(52) Ren, N.; Bosnar, S.; Bronić, J.; Dutour Sikirić, M.; Mišić, T.; Svetličić, V.; Subotić, B., Role of Subcolloidal (Nanosized) Precursor Species in the Early Stage of the Crystallization of Zeolites in Heterogeneous Systems. *Langmuir* **2014**, *30*, 8570-8579.

(53) Deman, A. J. M.; Vansanten, R. A., The Relation between Zeolite Framework Structure and Vibrational-Spectra. *Zeolites* **1992**, *12*, 269-279.

(54) Fan, F.; Sun, K.; Feng, Z.; Xia, H.; Han, B.; Lian, Y.; Ying, P.; Li, C., From Molecular Fragments to Crystals: A UV Raman Spectroscopic Study on the Mechanism of Fe-ZSM-5 Synthesis. *Chem.-Eur. J.* **2009**, *15*, 3268-3276.

(55) Chua, Y. T.; Stair, P. C., An ultraviolet Raman spectroscopic study of coke formation in methanol to hydrocarbons conversion over zeolite H-MFI. *J. Catal.* **2003**, *213*, 39-46.

(56) Fyfe, C. A.; Thomas, J. M.; Klinowski, J.; Gobbi, G. C., Magic-Angle-Spinning NMR (MAS-NMR) Spectroscopy and the Structure of Zeolites. *Angew. Chem., Int. Ed.* **1983**, *22*, 259-275.

(57) Van Grieken, R.; Sotelo, J. L.; Menendez, J. M.; Melero, J. A., Anomalous crystallization mechanism in the synthesis of nanocrystalline ZSM-5. *Microporous Mesoporous Mater.* **2000**, *39*, 135-147.

(58) Antonic, T.; Cifmek, A.; Kosanovic, C.; Subotic, B., Dissolution of Amorphous Aluminosilicate Zeolite Precursors in Alkaline Solutions. *J. Chem. Soc. Faraday Trans.* **1994**, *90*, 1973-1977.

(59) Nie, Y. Y.; Shang, S. N.; Xu, X.; Hua, W. M.; Yue, Y. H.; Gao, Z., In₂O₃-doped Pt/WO₃/ZrO₂ as a novel efficient catalyst for hydroisomerization of n-heptane. *Appl. Catal., A* **2012**, *433*, 69-74.

(60) Cha, S. H.; Byun, Y.; Min, H.-K.; Hong, S. B., 1,2,4-Trimethylbenzene disproportionation over large-pore zeolites: An experimental and theoretical study. *J. Catal.* **2015**, *323*, 145-157.

(61) Dimitrov, L.; Mihaylov, M.; Hadjiivanov, K.; Mavrodinova, V., Catalytic properties and acidity of ZSM-12 zeolite with different textures. *Microporous Mesoporous Mater.* **2011**, *143*, 291-301.

(62) Park, S. H.; Rhee, H. K., Shape selective conversion of 1,2,4-trimethylbenzene over zeolite NU-87. *Catal. Today* **2000**, *63*, 267-273.

(63) Roger, H. P.; Moller, K. P.; OConnor, C. T., The transformation of 1,2,4-trimethylbenzene - A probe reaction to monitor external surface modifications of HZSM-5? *Microporous Mater.* **1997**, *8*, 151-157.

Table of Content

